

Stellar Spectra A. - Basic Line Formation

AST4310

METIN SAN

14. September 2018

INTRODUCTION

Spectral lines in stellar spectra provide a wealth of knowledge about the studied object and its conditions and are therefore one of the most valuable sources of information to an astrophysicist. Spectral lines are dark lines which appear in continuous spectra as a result of absorption of light. In order to build an understanding of the information contained within a spectral line we will follow the work of Cecilia Payne and Marcel Minnaert, which were some of the early pioneers of spectral astronomy.

This report is split into two parts. In the first part we will recreate some of the work done by Cecilia Payne during her PhD thesis. This work will mainly consider statistical methods applied to study spectral lines, with a focus on Saha-Boltzmann modeling. The second part of the report will be more figure oriented where we consider *how* spectral lines form through the work of Marcel Minnaert. The programs used to create the following figures and results can be found on my github

[HTTPS://GITHUB.COM/METINSA/AST4310/TREE/MASTER/SSA](https://github.com/METINSA/AST4310/tree/master/SSA).

1. THE BOLTZMANN AND SAHA LAWS

Cecilia Payne (1900 - 1979) was a British-American astronomer and astrophysicist famous for showing that most stars are made of mainly hydrogen and helium. She applied the Saha distribution which was newly derived to stellar spectra. With this she was able to show that the empirical Harvard classification primarily represented a temperature scale.

In thermodynamical equilibrium, the equipartition laws Saha and Boltzmann describe the division of particles of a specific element. With the temperature as the only major parameter these laws show us how the different ionization stages and discrete energy levels of a specific element are distributed.

1.1 Boltzmann distribution

The Boltzmann distribution deals with how the energy levels is distributed, and is given by

$$\frac{n_{r,s}}{N_r} = \frac{g_{r,s}}{U_r} e^{-\chi_{r,s}/kT}, \quad (1)$$

where $n_{r,s}$ is the number density (also called level population) and $g_{r,s}$ the statistical weight of the level (r, s) where r is the ionization stage, and s is the state or level. $N_r = \sum_3 n_{r,s}$ is the total particle density over all levels of ionization. $\chi_{r,t}$ is the excitation energy measured from the ground state $(r, s = 1)$. The partition function U_r is defined by

$$U_r = \sum_s g_{r,s} e^{-\chi_{r,s}/kT}, \quad (2)$$

which consists of the same quantities found in the Boltzmann equation.

1.2 Strength ratio of α lines in hydrogen

Payne was studying the absorption lines in stellar spectra when she made the assumption that the strength of the absorption lines scaled with the population density of the lower level of the corresponding transition. If one assumes that most of the hydrogen resides in the lower energy levels, it follows that most transitions would result in higher energy levels. The strength of the lines should therefore scale with the population density of these lower levels. We know today that this assumption is not completely true, but stellar absorption lines do generally scale with larger lower-level populations. We will therefore proceed by assuming that Payne's assumption holds and that the scaling is linear.

This assumption allows us to estimate the strength ratios of the α lines of hydrogen, where α denotes that the excitation is from s to $s + 1$. For a neutral hydrogen atom ($r = 1$), the statistical weight goes as $g_{1,s} = 2s^2$, and the excitation energy goes as $\chi_{1,s} = 13.6(1 - 1/s^2)$. The ratio between Lyman α ($s = 1$) and Balmer α ($s = 2$) is then given from the Boltzmann equation (1) as

$$\frac{n_{1,1}}{n_{1,2}} = \frac{g_{1,1} e^{-\chi_{1,1}/kT}}{g_{1,2} e^{-\chi_{1,2}/kT}}, \quad (3)$$

where U_r and N_r have canceled out. We only need to insert for s and g in order to compare. By using the formula in equation (3) we can compute the strength ratio of the α lines in H I Lyman, Balmer, Paschen and Brackett series. For neutral hydrogen, the information needed is tabulated in table 1. Using the

information in this table we find that the following strength ratios for the solar temperature of 5770 K: (Lyman α / Balmer α) $\approx 2 \cdot 10^8$, (Balmer α / Paschen α) ≈ 20 , and (Balmer α / Brackett α) ≈ 42 . We see that Lyman α line strength is enormous compared to the other lines. This is a result of the excitation energy $\chi_{1,1} = 0$, making it temperature independent when computing ratios.

1.3 Saha distribution

The Saha distribution relates the ionization levels of an element in ionization equilibrium and is given by

$$\frac{N_{r+1}}{N_r} = \frac{1}{N_e} \frac{2U_{r+1}}{U_r} \left(\frac{2\pi m_e kT}{h^2} \right)^{3/2} e^{-\chi_r/kT}, \quad (4)$$

where m_e is the electron mass, h is Planck's constant N_e is the electron number density, and χ_r is the threshold ionization energy required to ionize from stage r to $r + 1$.

1.4 Element E (Schadeenium)

We will now consider the imaginary element E, or "Schadeenium". E is a simple atom which lets us evaluate Saha-Boltzmann statistics without having to bother about complex atomic data. It has the following properties:

- The statistical weight is $g_{r,s} = 1$ for all levels.
- For neutral E, the ionization energy is $\chi_1 = 7$ eV. For E^+ (ionized once) the energy is $\chi_2 = 16$ eV, and similarly $\chi_3 = 31$ eV and $\chi_4 = 51$ eV.
- The excitation energies increase incrementally by 1 eV: $\chi_{r,s} = s - 1$ eV.

We begin by computing the partition function U_r of E found in equation (2). The results is seen in figure 1.

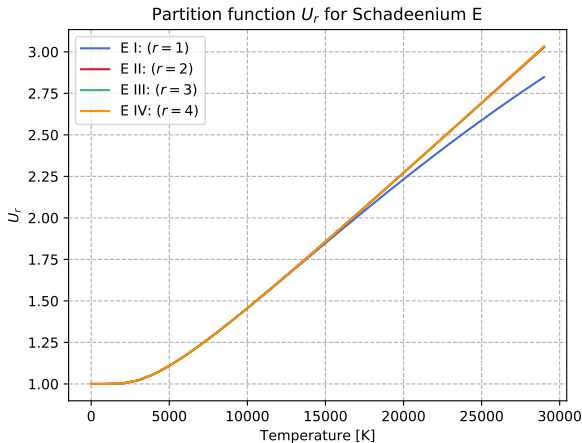


Figure 1: Partition function U_r for the imaginary element E.

We find that all ionizations mostly behave the same way for temperatures below 15000 K. For higher temperatures, U_1 splits from the other ionizations and

keeps a lower value. Generally we note that the partition function of element E is of order unity and appears to be weakly sensitive to temperature.

Further we can compare our calculation with Schadee's first table. We find that for $T = 5000$ K all ionizations have the value $U_r = 1.109$, which corresponds well to Schadee's $U_r = 1.11$. For $T = 10000$ K we find that again all ionizations have more or less the same value of $U_r = 1.456$, which can be rounded up to Schadee's $U_r = 1.46$. Finally for $T = 20000$ K we find that $U_1 = 2.232$ and $U_2 = U_3 = U_4 = 2.271$, where as Schadee tabulated $U_1 = 2.27$, and $U_2 = U_3 = U_4 = 2.27$. We see that these values correspond nearly perfectly to those tabulated by Schadee.

Line α	s	$\chi_{1,s}$ [eV]	$g_{1,s}$
Lyman	1	0	2
Balmer	2	10.20	8
Paschen	3	12.09	18
Brackett	4	12.75	32

Table 1: Neutral hydrogen information

1.4.1 Boltzmann distribution for E

With the partition function calculated, we can study the Boltzmann distribution for E. This is done by computing the boltzmann equation (1) for varies levels s . The result can be seen in figure 2.

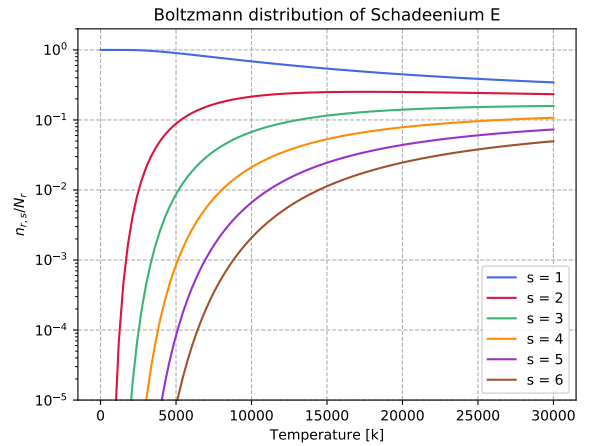


Figure 2: Boltzmann distribution of the imaginary element E.

By studying figure 2 we notice that in thermal equilibrium, for all temperatures, the ground state always has the largest population. At $T = 5000$ K we have $n_{r,s}/N_r = 0.9$ for $s = 1$ and $n_{r,s}/N_r \approx 0.09$ for $s = 2$ and so on for the lower levels which perfectly corresponds to those tabulated by Schadee. We see that all these add up to unity for all temperatures, which is a results off the scaling by N_r . We can conclude that the lowest levels are the most important ones which is a result of the rapid decay of the Boltzmann factor $e^{-\chi_{r,s}/kT}$. For the ground state the excitation energy

$\chi_{r,0} = 0$ which explains why the ground state never experiences the steep decay.

1.4.2 Saha distribution for E

We will now study the Saha distribution of the element E. By computing the saha equation (4) for varying ionizations we obtain the results seen in figure 3.

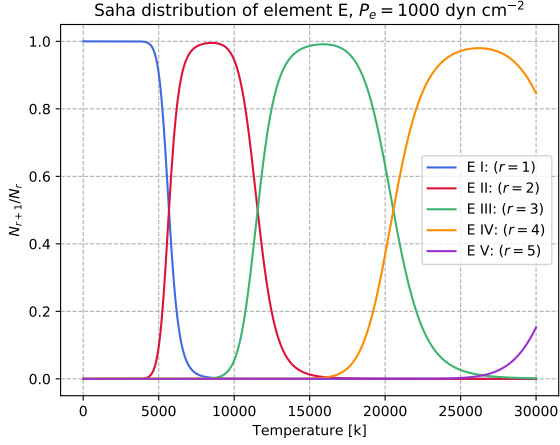


Figure 3: Saha distribution of the imaginary element E with an electron pressure of $P = 1000 \text{ dyn cm}^{-2}$.

Since this is a normalized distribution in the same way as the Boltzmann distribution, the ionizations always add up to one. We also notice that for solar temperatures, only 2 ionizations are significantly present. At $T = 5000$ we see that $N_{r+1}/N_r \approx 0.91$ for $r = 1$, while $N_{r+1}/N_r \approx 0.089$ for $r = 2$, while the higher ionization stages are negligible. This means that for solar temperatures, E is mostly neutral. For higher temperatures around $T = 10000 \text{ K}$, we find that $N_{r+1}/N_r \approx 0.95$ for $r = 2$ and $N_{r+1}/N_r \approx 0.05$ for $r = 3$, while the other ionizations are again negligible. This suggests that there are at all times mainly 2 ionizations stages present in a gas at a given temperature.

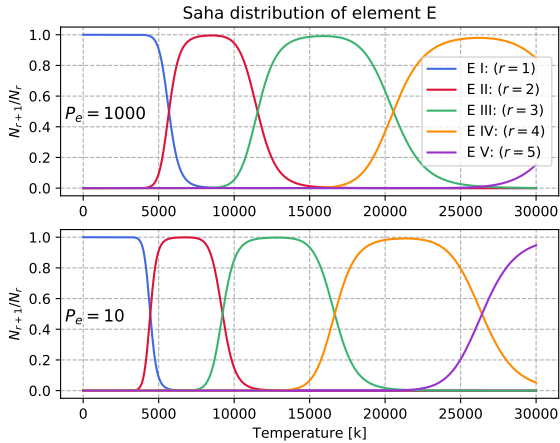


Figure 4: Saha distribution of the imaginary element E for two different electron pressures. Upper plot: $P_e = 1000$. Lower plot: $P_e = 10$.

We can also study what effects the electron pressure has on the saha distribution. The electron number density N_e can be written as $N_e = P_e/kT$ if one assumes ideal gas. We do so by computing the saha equation (4) for two values of P_e . The results of this can be seen in figure 4.

Figure 4 shows the difference P_e makes when computing the Saha distribution. We note that in the lower subplot with $P_e = 10$ the distribution seems to have been squished towards the left. This means that ionization occurs at earlier temperatures for low values of electron pressure.

We note that the Boltzmann and Saha distributions behave differently for increasing temperatures. The Boltzmann equation converges to $g_{r,s}/U_r$ as $T \rightarrow \infty$. The same is not true for the Saha distribution. The two distributions share the term $e^{-\chi/kT}$ term which converges to 1 as $T \rightarrow \infty$. However, the Saha distribution has a factor $T^{3/2}$ which grows exponentially as T increases. This is the factor that separates the two distributions.

1.4.3 Payne curves for E

The underlying premise in Payne's analysis was that one might expect that the observed strength of a spectral line involving level (r, s) scales with the Saha-Boltzmann prediction for the lower level population $n_{r,s}$ (if Thermodynamical equilibrium holds). We will study this as Payne did by computing the product of the two distributions in question and then plotting the results in a Payne-like graph.

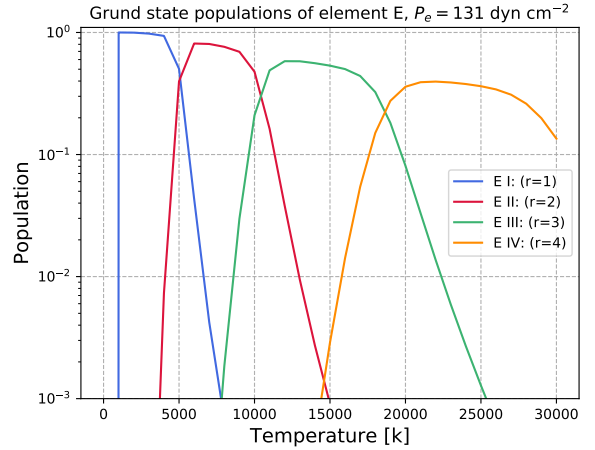


Figure 5: Saha-Boltzmann distribution ground state populations for E.

We start by computing and plotting the ground state populations ($s = 1$) for E with an electron pressure of $P_e = 131 \text{ dyn cm}^2$. The result is seen in figure 5

Figure 5 shows the so called Payne curves of the ground state population of E. Its easy to recognize that this plot as a product of the Saha and Boltzmann distributions. We note that the maximum amplitude decreases with increasing ionization which is a result

of the Boltzmann distribution. The steep flanks on the left and right side are a result of the Saha distribution behaviour. We also see that the flanks get less steep as $T \rightarrow \infty$ which is also the case in the Saha distribution seen in 4. Similarly, for temperatures greater than 15000 K, most if not all atoms will be E II.

We will further study the influence of the Boltzmann factor by adding curves of higher values of excitation states s . By including excitation levels up to $s = 4$, we find the following result seen in figure 6.

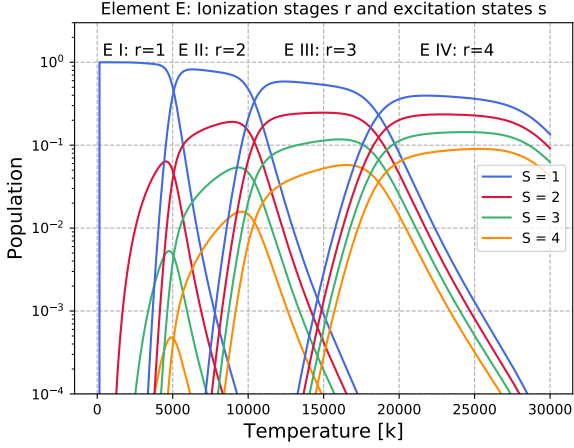


Figure 6: Payne curves for element E for various energy levels s .

First of all we notice that the ground state ($s = 1$) dominate the population for all ionizations and across all temperatures. However, as $T \rightarrow \infty$ the ground state population of the different ionizations gets smaller, meaning that the population is distributed more evenly over the different states. In general we see that the population moves to higher energies for high temperatures.

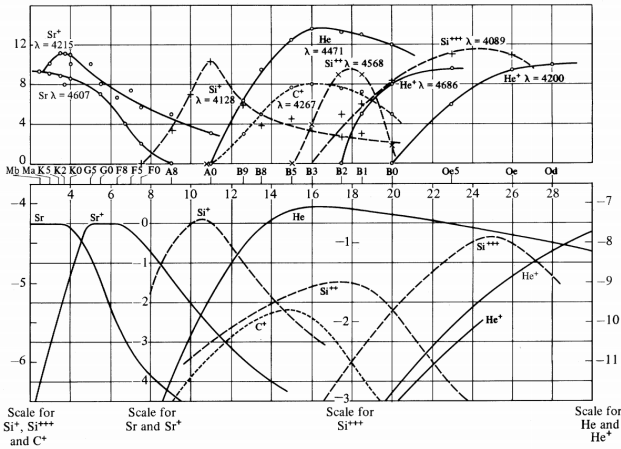


Figure 7: The original Payne curves (1924). Upper panel displays the variations of observed line strengths. Lower panel displays the Saha-Boltzmann distribution.

Our produced results in figure 6 are comparable to

those of Payne seen in the lower panel of 7. In order to reproduce her results more closely we would need to evaluate the equations for the actual elements she used instead of E. Her results are plotted as a function of the Harvard classification of stellar spectra, while our is a function of temperature. Payne's conclusion was therefore that the Harvard classification is primarily an ordering of temperature based on the Saha-Boltzmann population statistics.

1.5 Hydrogen H I (and Ca⁺ K)

We will now extend our Saha-Boltzmann analysis to neutral hydrogen H I. Hydrogen is a bit more complex than the imaginary element E, but still fairly simple. It has the following properties

- Ionization energy $\chi_1 = 13.598$ eV
- Statistical weight $g_{1,s} = 2s^2$
- Level energy $\chi_{1,s} = 13.598(1 - 1/s^2)$ eV
- Single ion stage $U_2 = g_{2,1} = 1$

In addition to hydrogen, we will also study the calcium line Ca⁺ K. The Ca⁺ K line behaves in the same way as element E for $r = 2$ and $s = 1$ with an exception of a factor 2 which makes for an easy calculation as we already have the Saha-Boltzmann routine for E. It does have slightly different ionization energies however, so that $\chi_1 = 6$, $\chi_2 = 12$, $\chi_3 = 51$, $\chi_4 = 67$.

1.5.1 Saha-Boltzmann population of H I and Ca⁺ K

By using the new information for Hydrogen and Ca⁺, we have computed the Saha-Boltzmann distribution which can be seen in figure 8

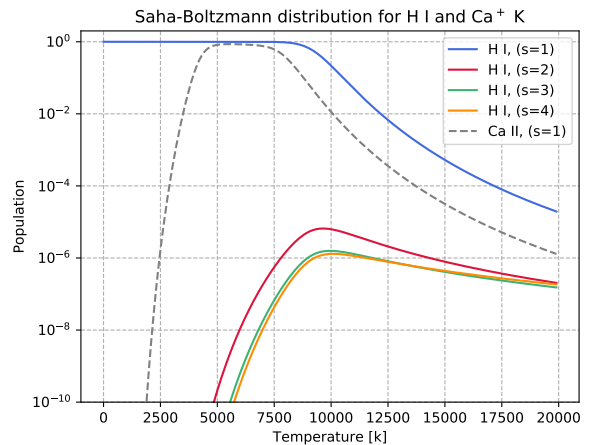


Figure 8: Saha-Boltzmann distribution of H I and Ca⁺ K.

We will ignore the Ca⁺ K population to begin with. By comparing the Saha-Boltzmann distribution for H I and E I, seen in figure 6, we see that there are some similarities. The main difference being that H I seems to fall off more slowly for higher temperatures.

1.5.2 Solar $H\alpha$ versus $Ca^+ K$: Line strength

If one studies the spectrum of the sun, as Payne did, one notices that the $Ca^+ K$ spectral line is much stronger than the hydrogen α lines. This is strongly contradictory to the previous assumption made which says that the strength of the absorption lines scaled with the population density as one knows that hydrogen is massively more abundant than calcium ($N_{Ca}/N_H = 2 \times 10^{-6}$).

However, the $H\alpha$ line is a $s = 2 \rightarrow 3$ transition, and by studying the Saha-Boltzmann distribution in figure 8 we see that the $H I (S = 2)$ abundance at solar temperatures is of order 10^{-10} . The $Ca^+ K$ has the ground state as its lower transition, and has therefore the dominating population, which means that the assumption still holds.

We can prove this by computing the expected strength ratio of these two lines as a function of temperature. We find this ratio by multiplying the calcium abundance with the Saha-Boltzmann ratio of the two elements. The result is then plotted in figure 9.

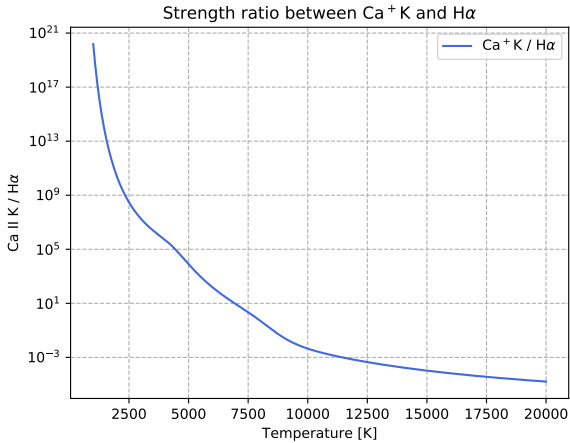


Figure 9: Solar line strength ratio $Ca^+ K / H\alpha$ with $P_e = 100 \text{ dyn cm}^2$

At low temperatures we observe a complete domination by the calcium line. However, we see that the ratio exponentially weakens as the temperature increases. This is expected as there are more and more hydrogen atoms that get ionized, which leads to a higher $H II$ abundance.

1.5.3 $H\alpha$ vs $Ca^+ K$: Temperature sensitivity

It is of interest to study how the two lines differ in their temperature sensitivity. We can do so by computing and plotting the relative population changes

$$\frac{(\Delta n_{Ca}/\Delta T)}{n_{Ca}} \quad \text{and} \quad \frac{(\Delta n_H/\Delta T)}{n_H},$$

where ΔT is a small temperature change. The result can be seen in the upper panel in figure 10, where we have also plotted each population in relative units in the lower panel.

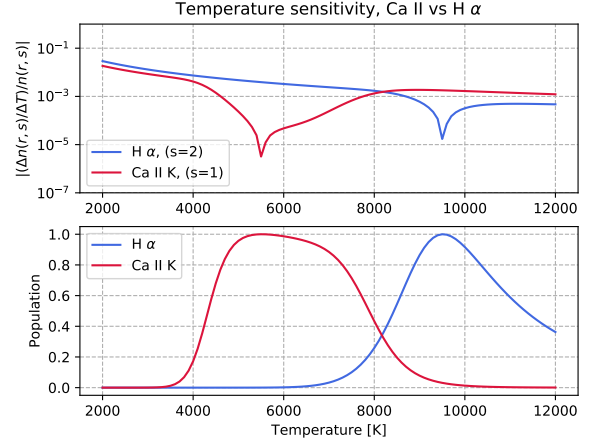


Figure 10: Upper panel: Temperature sensitivity of $Ca II$ and $H\alpha$. Lower panel: Relative population of the corresponding elements.

From figure 10 we notice that both lines start off with roughly the same sensitivity. We spot two dips in the temperature sensitivity. One for $Ca II$ around 5600 K, and one for $H\alpha$ around 9500 K. The dips seem to occur once the population of each respective line reach their maxima. This can be interpreted as the sensitivity being at its highest when the population experience change. Similarly, the sensitivity experiences a rapid drop for the short temperature range where the population remains constant at the maxima.

The temperature sensitivity is essentially in some way the derivative of the population with respect to temperature. We see that the temperature sensitivity decreases at the left flank, so that $\Delta n < 0$, while the opposite is true at the right flank $\Delta n > 0$.

We also note that $H\alpha$ is the more temperature sensitive line for temperatures which corresponds to those of the solar photosphere.

1.5.4 Hot stars versus cool stars

One last interesting topic is when it comes to Payne's work is the definition of "hot" and "cool" stars. The transition between a hot and a cool star is defined to be where 50% of the hydrogen is ionized. We can then study at which temperature the Sun's photosphere would require to be classified as a hot star. We do so by computing the Saha-Boltzmann distribution of the neutral hydrogen and extract the temperature at which the fraction equals 0.5.

The results of this can be seen in figure 11. We observe that the point where the hydrogen is 50% ionized has a temperature of $T = 9213 \text{ K}$. We have also plotted a vertical line through this point which denotes the transition between hot and cool stars. Cool stars get their electrons mostly from metals, while hot stars get their electrons from the ionized hydrogen.

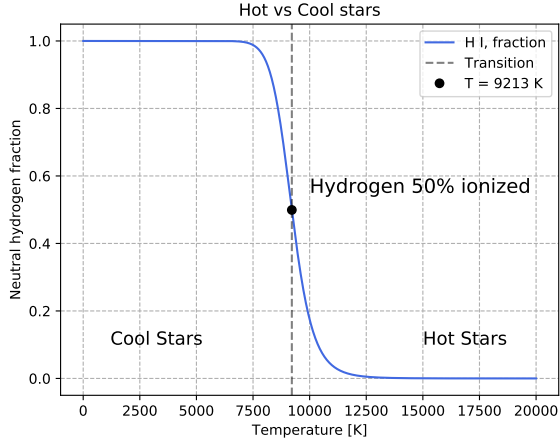


Figure 11: Saha-Boltzmann distribution of H I displaying the transition between "hot" and "cool" stars.

1.6 Conclusion / Discussion to part 1

Most of the results have been discussed through out the report, but we will give a short summary. By recreating the work of Cecilia Payne, we have learned about the statistical distributions that govern the behavior of stellar spectra. We have seen how the energy levels of the atoms in stellar objects are distributed through the Boltzmann equation. We have also looked at how the ionization population changes with temperature through studying the Saha distribution. We have then seen that combining these two distributions result in a Payne-like graph which gives a good overview of properties we would expect to see by studying stellar objects. By comparing our "Payne-curves" to observations done, we can see that the Harvard classification is a ordering of temperature based on these statistics. These statistics can also be applied to study strenght ratios between different lines and define "Hot" and "Cool" stars.

2. THE ORIGIN OF SPECTRAL LINES

In part one we discussed the laws governing the material in stellar bodies. We will now move on to the radiation counterpart to the material and study how the spectral lines found in stellar spectra are formed.

2.1 Planck's law

The Planck function specifies the intensity of electromagnetic radiation emitted by a black body in thermal equilibrium for a given temperature T . The function is given as

$$B_{\lambda}(T) = \frac{2hc^2}{\lambda^5} \frac{1}{e^{hc/\lambda kT} - 1}, \quad (5)$$

where c is the speed of light, h is Planck's constant, λ is the wavelength and T is the temperature. B_{λ} has dimension $\text{erg cm}^{-2} \text{s}^{-1} \text{cm}^{-1} \text{steradian}^{-1}$ in cgs units.

We can compute the Planck law for wavelengths in the visible spectrum (1000 - 20800 Å for temperatures $T \in [5000, 8000] \text{K}$). This is then plotted in three separate figures, figure 12, figure 13 which shows the Planck law with a logarithmic y-scale and figure 14 which shows the Planck law in a loglog plot.

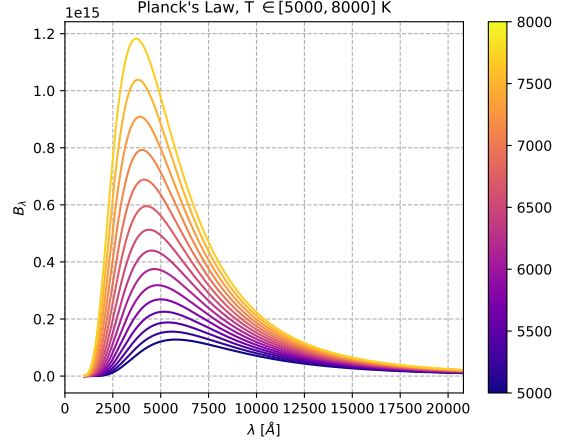


Figure 12: Planck's law for wavelengths λ in the visible spectrum for [Å]. The colorbar denotes the temperature, T . B_{λ} increase with temperature at all wavelengths with the maximum intensity of each temperature occurring at the low ends of the wavelengths. We note that the maximas are slightly shifted towards lower wavelengths for higher temperatures.

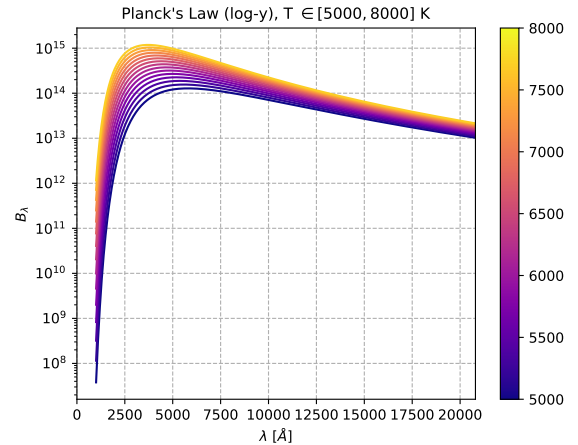


Figure 13: Planck's law for wavelengths in the visible spectrum with logarithmic y scale. We see that it is easier to interpret the magnitude of the intensity for the different wavelengths in this format. We see that for some very small wavelengths B_{λ} drops down to below 10^8 . We can also see that each temperature has a different initial intensity. We also see that large wavelengths do in general have more intensity than the very small wavelengths (even though the maxima occurs at relatively small wavelengths). It's also easier to see that the maximas are shifted towards lower wavelengths for higher temperatures in this format.

We notice that B_λ increases with temperature at any wavelength but faster towards the Wien regime. This is the regime where the Wien approximation or Wiens law holds. Figure 15 and figure 16 shows Planck's law in addition to the two approximations in Wien and Rayleigh-Jeans law's. We see that the Wien approximation is spot on for both the left and upper-most side of the Planck curve (low wavelengths). This region is therefore called the Wien regime. Figure 16 shows us the region where the Rayleigh-Jeans approximation is the best fit, which is at the right side of the Planck curve (high wavelengths).

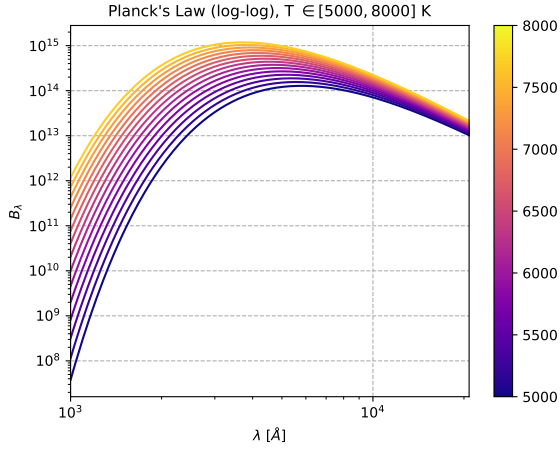


Figure 14: Planck's law for wavelengths in the visible spectrum with logarithmic x and y scale. Plotting the law in a loglog plot displays a different curvature compared to two previous figures. low wavelengths with different temperatures are separated further from each other and can more easily be studied.

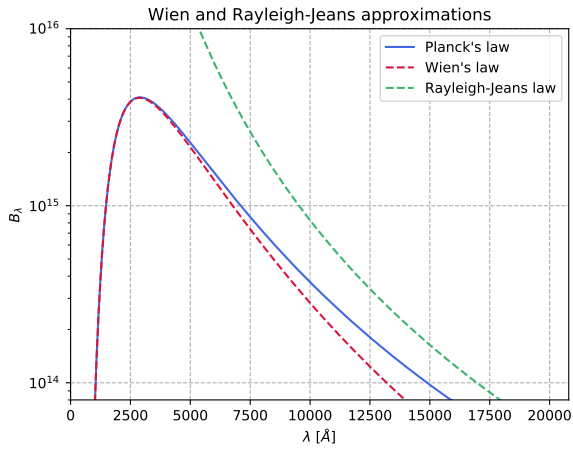


Figure 15: Planck's, Wien's and Rayleigh-Jeans law plotted in the same figure. This figure shows that Wien's approximation is accurate at the regime of low wavelengths λ (Wien regime).

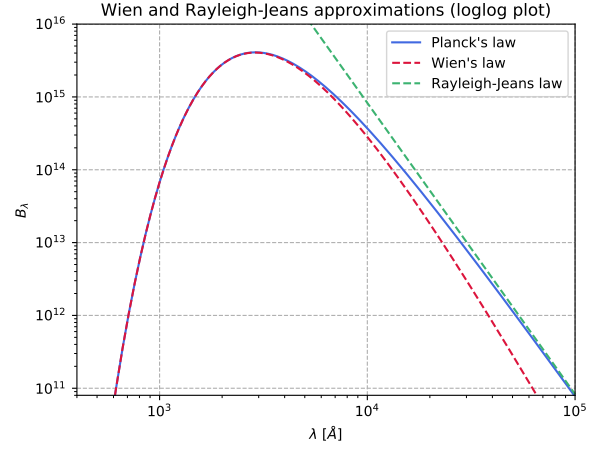


Figure 16: Planck's, Wien's and Rayleigh-Jeans law plotted in the same figure. This figure shows that Rayleigh-Jeans approximation is accurate at the regime of high wavelengths λ (Rayleigh-Jeans regime) as it converges towards Planck's law for high wavelengths while Wien's approximation diverges

2.2 Radiation through isothermal layer

We will now study a beam of radiation intensity $I(0)$ that passes through a layer. Depending of the features of this layer, the emerging intensity will be attenuated by absorption. The weakened intensity that emerges from the layer is given by $I = I(0)e^{-\tau}$, where τ , also called the "optical thickness" is the decay parameter which specifies total opaqueness.

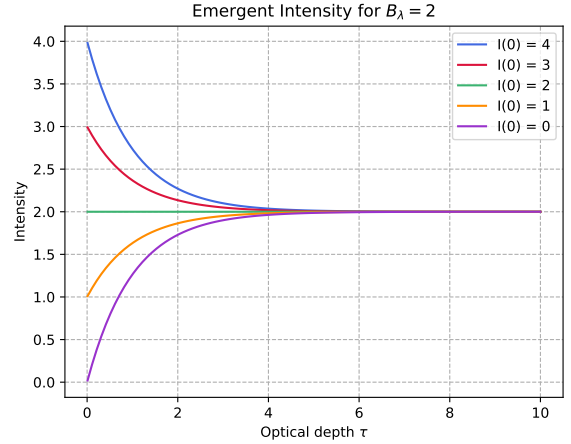


Figure 17: Intensity I_λ plotted for optical depth $\tau \in [0, 10]$ for 5 different initial intensities $I(0)$. We have used $B_\lambda = 2$ which is the intensity originating from the layer. For $\tau \gg 1$ nothing comes through the layer, while everything comes through if $\tau \ll 1$. This can be seen if one looks at $\tau = 0$, where we see that the emergent intensity is equal to the initial intensity. We also see that optically thin layers generate next to non intensity by themselves. All intensities end up converging to B_λ for $\tau \gg 1$.

We also need to account for the radiation that

originated from within the layer itself. This is locally given as $\Delta I = B_\lambda(T)\Delta\tau$. It can then be shown that the total emergent radiation from a layer is given as

$$I_\lambda = I_\lambda(0)e^{-\tau} + \int_0^\tau B_\lambda[T(x)]e^{-(\tau-\tau(x))}, \quad (6)$$

which for an isothermal layer (the type we will consider here) can be reduced to

$$I_\lambda = I_\lambda(0)e^{-\tau} + B_\lambda(1 - e^{-\tau}). \quad (7)$$

We can study this by plotting the intensity. This can be seen in figures 17 and 18.

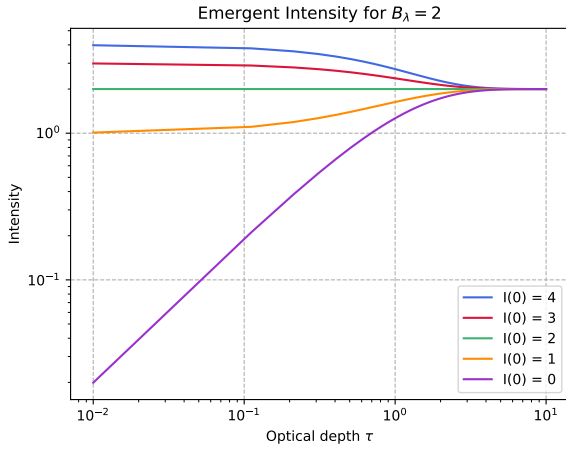


Figure 18: This figure shows the results of figure 17 plotted in a log-log plot which allows us to study what happens for $\tau \ll 1$. We see that even for $I(0) = 0$ (no incoming radiation), the layer still emits some radiation as long as the layer has an optical depth. As the depth increases, the layer radiates more and more intensity, which eventually converges at the source intensity B_λ .

2.3 Schuster-Schwarzschild model and Voigt profile

We will now apply the results from the isothermal layer to a simple solar model, the Schuster-Schwarzschild model. In this model, the emergent radiation of the line wavelengths is given by

$$I_\lambda = B_\lambda(T_{\text{surface}}e^{-\tau_\lambda}) + B_\lambda(T_{\text{layer}})(1 - e^{-\tau_\lambda}), \quad (8)$$

where we see that the opaqueness τ in (8) has been indexed with λ . This is because the optical depth varies over the spectral line which results in line broadening. This broadening can be described through the distribution

$$\tau(u) = \tau(0)V(a, u), \quad (9)$$

where V is the Voigt function and the parameters a and u represent the dampening and wavelength separation. The Voigt function is defined through the convolution of a Gauss profile with a Lorentz profile, and can be approximated to read

$$V(a, u) \approx \frac{1}{\Delta\lambda_D\sqrt{\pi}} \left[e^{-u^2} + \frac{a}{\sqrt{\pi}u^2} \right]. \quad (10)$$

We will study the Voigt function by plotting it in the range $u \in [-10, 10]$ for $a = 0.1$, $a = 0.01$, $a = 0.001$ and $a = 0.0001$. The results are seen in figures 19 and 20.

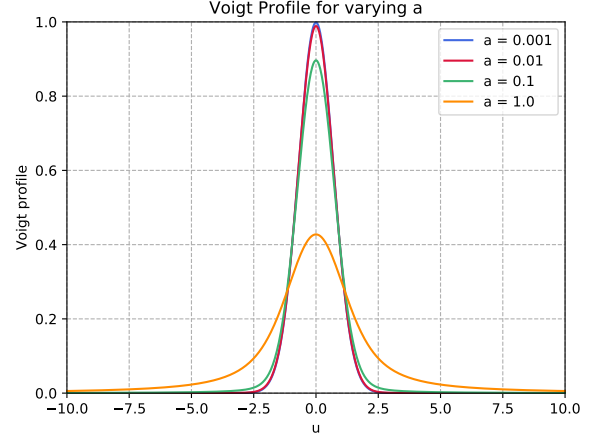


Figure 19: Voigt profile approximation for varying levels of dampening. We see that the profiles have an amplitude around $u = 0$. This can be seen from the approximation (10) where we see that both terms in the bracket decrease as $\pm u$ deviate from 0. We also note that the amplitude of the profiles increase with smaller values of a . This seems to contradict the approximation from which one would think the profile would decrease with a . The left term in the bracketed also seems to pose problems when u becomes 0 as the term would become infinity.

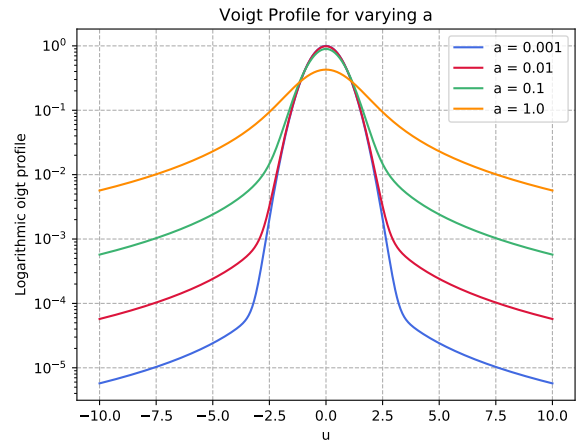


Figure 20: This figure shows the Voigt profile with logarithmic y-scale. This lets us inspect the behaviour of the outer wings of the profile. We see that different values of a also results in the profile converging at different values. Smaller a values result in smaller end values, which matches the approximation.

2.4 Emergent line profiles

By combining the Schuster-Schwarzschild model seen in equation (8) with the Voigt profile, we are able to compute and plot stellar spectral lines. We compute these line profiles for solar photosphere values as seen in the optical part of the spectrum. The results are seen in figures 21, 22, 23 and 24.

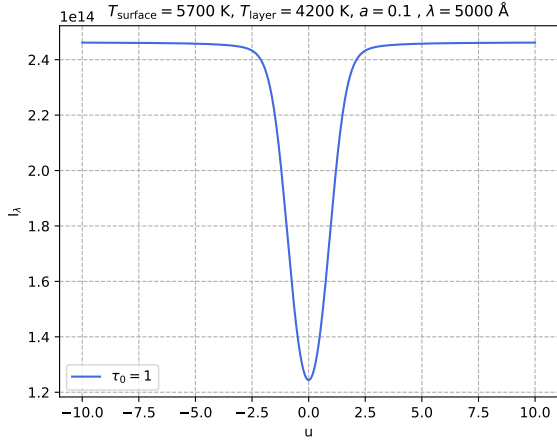


Figure 21: Schuster-Schwarzschild line profile with optical depth $\tau_0 = 1$ using solar values included in plot title. We see that the shape of the curve resembles an inverted Voigt profile which makes sense as we use a combination of the Voigt profile and Schuster-Schwarzschild model.

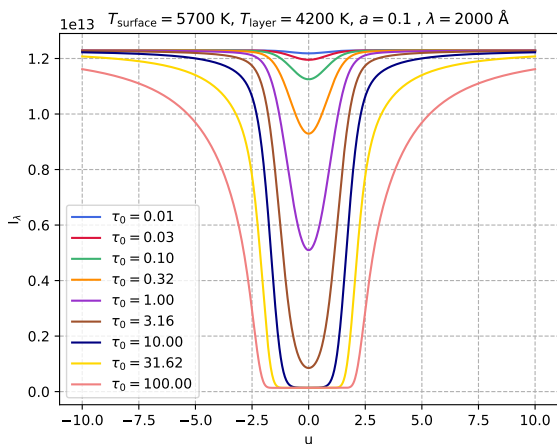


Figure 22: Schuster-Schwarzschild line profile for varying values of the optical depth τ_0 . We spot that for optically thin $\tau_0 \ll 1$, almost non of the intensity gets absorbed, while for optically thick $\tau_0 \gg 1$, all the intensity gets absorbed, and we only remain with the layer source intensity. We also note that the spectral lines broaden with increasing optical depth.

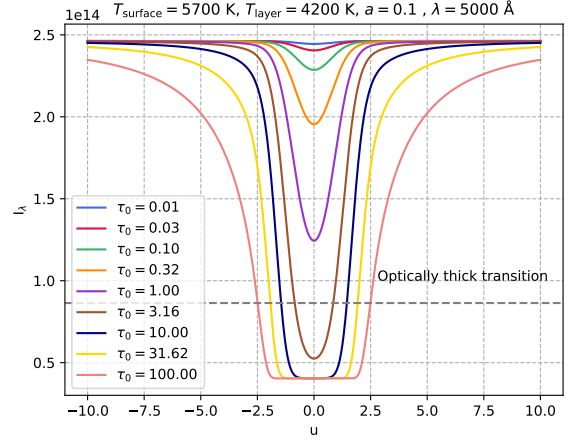


Figure 23: Schuster-Schwarzschild line profile for $\lambda = 5000$. If one defines a optically thick layer to be $\tau = 1$, then we see that a medium is optically thick if the emergent intensity has been reduced by $1/e$. In the case of this plot with $\lambda = 5000$ Å, the initial intensity is 2.34×10^{14} which means that once a value τ_0 results in the intensity at the minima dropping below 8.63×10^{13} , that value of τ_0 would be the transition. In our case that would be somewhere around $\tau_0 \approx 2$. We also see that at $u = 5$, all spectral lines are above the transition layer and is optically thin.

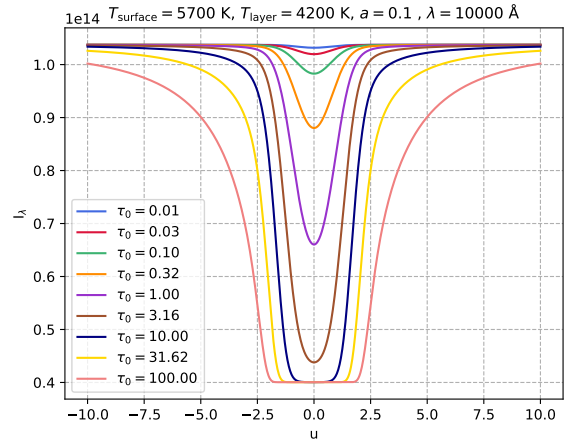


Figure 24: Schuster-Schwarzschild line profile for $\lambda = 10000$. Wavelength analysis: We see that the wavelength has an effect on the intensity. We see that for $\lambda = 2000$ Å, the intensity continuum intensity is the lowest and the highest for $\lambda = 5000$. $\lambda = 10000$ is quite low, but not as low as for $\lambda = 2000$. This is of-course connected to Planck's law. We see from figure 12 that for temperatures around 5000 K, the intensity peak lies on around $\lambda \approx 4000$.

2.5 Equivalent width of spectral lines

Minnaert together with his coworkers introduced the *equivalent width* W_λ as a line-strength parameter which measures the growth quantitatively. This quantity measures the integrated line depression in the nor-

malized spectrum, and is given as

$$W_\lambda = \int \frac{I_{\text{cont}} - I(\lambda)}{I_{\text{cont}}} d\lambda. \quad (11)$$

Numerically, we compute this by summing $(I_\lambda - I(0))d\lambda/I_\lambda$, where $d\lambda$ is the steplength in the wavelength array. Doing will compute the equivalent width for the Schuster-Schwarzschild profile seen in figure 25, we get the result seen in figure 26.

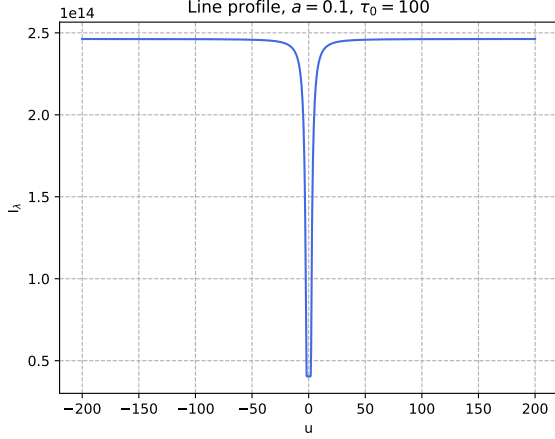


Figure 25: Schuster-Schwarzschild line profile for $\lambda = 5000 \text{ \AA}$. This is the same result as the $\tau_0 = 100$ seen in figure 23, with the only difference being the u range on the x-axis which results in a thinner looking profile.

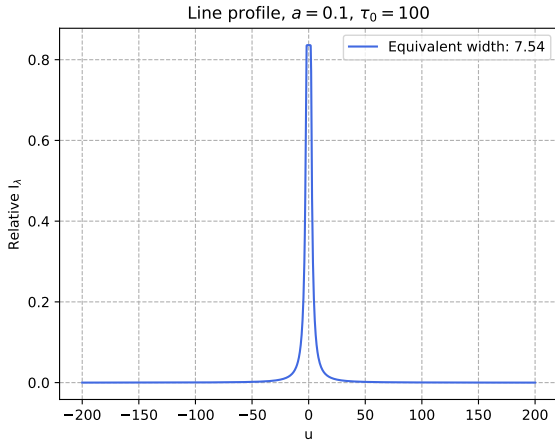


Figure 26: Relative intensity of line profile from figure 25. This relative intensity only considers the difference in intensity from the continuum's intensity which results in an inverted figure. We have also normalized by dividing by I_{cont} . The equivalent width is then computed using equation (11).

2.6 Curve of growth

The main purpose of the equivalent width is that it can be used to measure the number of atoms in the reversing layer. From our profile plots we have illustrated that the intensity growth is only linear for

$\tau_0 \ll 0$. In order to full growth of the line or the "curve of growth" we will plot W_λ against $\log \tau_0$. The result of this can be seen in figures 27 and 28.

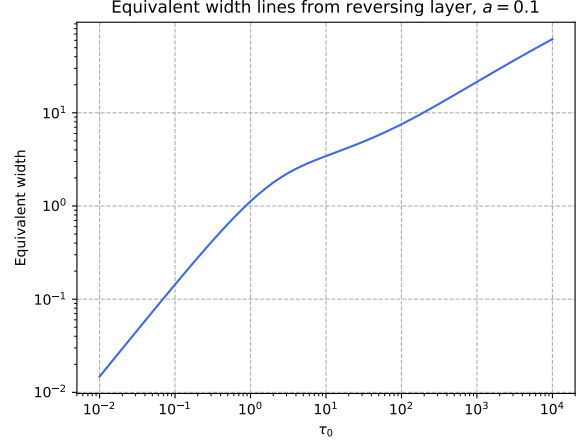


Figure 27: Equivalent width W_λ plotted for $\tau_0 \in [10^{-2}, 10^4]$. We see that the first part of the curve is linear 1:1. This is because we are in the $\tau_0 \ll 1$ regime, and from figure 18, we know that this is linear. This continues till we reach $\tau_0 = 1$, where the curve now becomes 1:2. This slope continues until we hit the $\tau_0 \gg 1$ regime. Here the curve slope increases again, but not as much as in the $\tau_0 \ll 1$ regime.

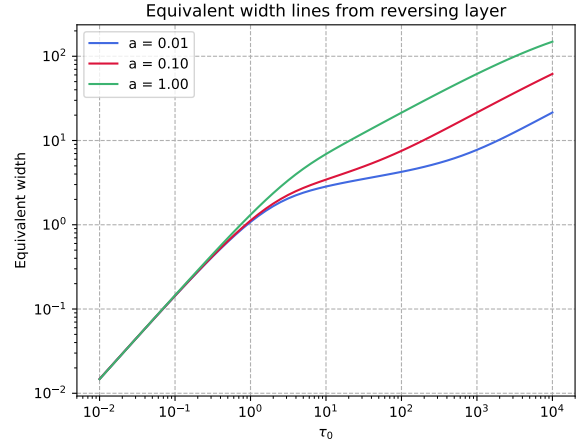


Figure 28: Similar equivalent width plot as in figure 27, but now with varying values of the damping parameter a . We see that change this parameter changes the behaviour of the the non $\tau_0 \ll 1$ regime. One can compare the curve of growth with the empirical curve of growth for the solar iron lines by tuning this parameter. By comparing the two curves we find that the solar iron lines has a damping parameter roughly in between $a = 0.01$ and $a = 0.1$.

Finally, we note that if one wants to produce emission lines rather than absorption, one needs to tune the temperatures used. We find that if $T_{\text{surface}} > T_{\text{layer}}$ we get absorption, if the opposite is true, we

get emission. The emission line produces by changing this up is seen in figure 29, and the corresponding growth curve in figure 30.

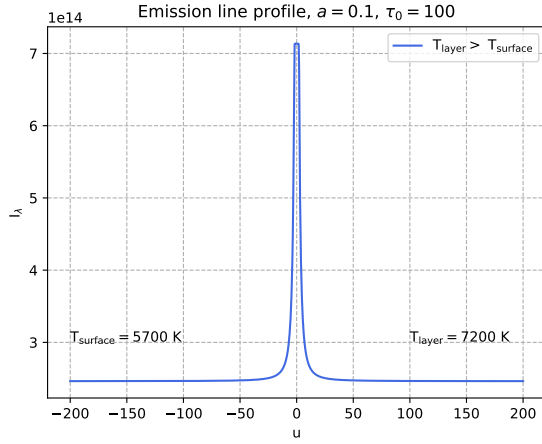


Figure 29: We have replotted the Schuster-Schwarzschild line profile with $\lambda = 5000 \text{ \AA}$, seen in figure 25, but now with a layer temperature of 7200 K. We see that this results in emission lines instead of absorption lines.

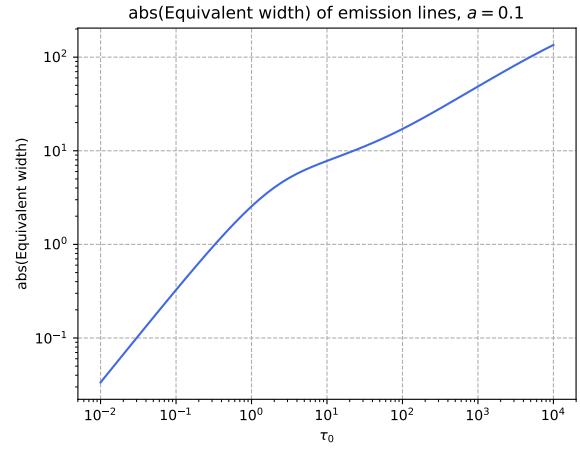


Figure 30: Curve of Growth for the emission line in figure 29 . We have computed the absolute value of the equivalent width in order to not get negative values. We see that the curve very much resembles that of the absorption line.